

JGR Space Physics

RESEARCH ARTICLE

10.1029/2021JA029742

Special Section:

Cluster 20th anniversary: results from the first 3D mission

Key Points:

- We demonstrate a novel technique to quantify the polar cap plasma circulation statistically
- During local summer and by dominated Interplanetary Magnetic Field (IMF), lobe reconnection is estimated to amount to ~20% of the dayside reconnection rate
- In the local summer hemisphere, dayside polar cap convection is more vortical compared to the local winter hemisphere during IMF B_y periods

Correspondence to:









J. P. Reistad,
jone.reistad@uib.no

Citation:

Reistad, J. P., Laundal, K. M., Østgaard, N., Ohma, A., Burrell, A. G., Hatch, S. M., et al. (2021). Quantifying the lobe reconnection rate during dominant IMF B_y periods and different dipole tilt orientations. *Journal of Geophysical Research: Space Physics*, 126, e2021JA029742. <https://doi.org/10.1029/2021JA029742>

Received 2 JUL 2021
Accepted 29 OCT 2021

Quantifying the Lobe Reconnection Rate During Dominant IMF B_y Periods and Different Dipole Tilt Orientations

J. P. Reistad¹ , K. M. Laundal¹ , N. Østgaard¹ , A. Ohma¹ , A. G. Burrell² , S. M. Hatch¹ , S. Haaland^{3,1,4} , and E. G. Thomas⁵ 

¹Birkeland Centre for Space Science, University of Bergen, Bergen, Norway, ²Space Science Division, U.S. Naval Research Laboratory, Washington, DC, USA, ³Max Planck Institute for Solar System Research, Göttingen, Germany, ⁴The University Centre in Svalbard, Longyearbyen, Svalbard, ⁵Thayer School of Engineering, Dartmouth College, Hanover, NH, USA

Abstract Lobe reconnection is usually thought to play an important role in geospace dynamics only when the Interplanetary Magnetic Field (IMF) is mainly northward. This is because the most common and unambiguous signature of lobe reconnection is the strong sunward convection in the polar cap ionosphere observed during these conditions. During more typical conditions, when the IMF is mainly oriented in a dawn-dusk direction, plasma flows initiated by dayside and lobe reconnection both map to high-latitude ionospheric locations in close proximity to each other on the dayside. This makes the distinction of the source of the observed dayside polar cap convection ambiguous, as the flow magnitude and direction are similar from the two topologically different source regions. We here overcome this challenge by normalizing the ionospheric convection observed by the Super Dual Aurora Radar Network (SuperDARN) to the polar cap boundary, inferred from simultaneous observations from the Active Magnetosphere and Planetary Electrodynamics Response Experiment (AMPERE). This new method enable us to separate and quantify the relative contribution of both lobe reconnection and dayside/ nightside (Dungey cycle) reconnection during periods of dominating IMF B_y . Our main findings are twofold. First, the lobe reconnection rate can typically account for 20% of the Dungey cycle flux transport during local summer when IMF B_y is dominating and IMF $B_z \geq 0$. Second, the dayside convection relative to the open/closed boundary is vastly different in local summer versus local winter, as defined by the dipole tilt angle.

Plain Language Summary Reconnection of magnetic field lines at high latitudes, tailward of the magnetic poles, is most often thought to play a big role in near-Earth space dynamics only when the magnetic field carried by the solar wind, the Interplanetary Magnetic Field or IMF, has a large northward component. This is because such conditions lead to the distinct strong sunward movement of plasma at polar latitudes in the ionosphere. During more typical conditions (when the IMF is dawn/dusk directed), identifying and quantifying the effect of such high-latitude reconnection becomes much more challenging. This paper presents a new technique that enables this separation even when the dawn-dusk component of the IMF is dominating, by normalizing the convection to the boundary between open and closed magnetic field lines. We make two main findings. First, the summer and winter dayside plasma flows near the boundary between open and closed magnetic field lines are vastly different. Second, plasma circulation at polar latitudes (interpreted as lobe reconnection rate) can on average account for ~20% of the total plasma transport during local summer when IMF is mostly directed in the dawn-dusk direction and IMF B_z is northward.

1. Introduction

It is well known that the Interplanetary Magnetic Field (IMF) has profound effects on the plasma circulation pattern throughout the outer parts of the Earth's magnetosphere. This circulation is explained by means of a cycle of dayside and subsequently nightside reconnection, known as the Dungey cycle. The plasma circulation is manifested also in ionospheric convection at high latitudes. Hence, the large-scale ionospheric convection pattern has been widely used to infer properties of the more distant solar wind-magnetosphere

©2021. The Authors.

This is an open access article under the terms of the [Creative Commons Attribution License](https://creativecommons.org/licenses/by/4.0/), which permits use, distribution and reproduction in any medium, provided the original work is properly cited.

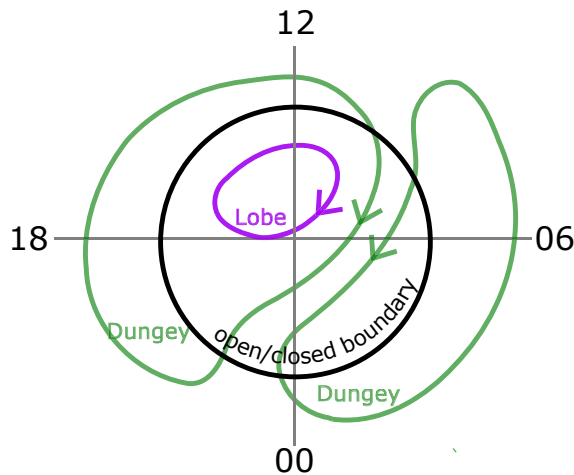


Figure 1. Conceptual illustration of the high-latitude ionospheric convection relative to the open/closed field line boundary for a B_y dominated interplanetary magnetic field (IMF). The open/closed field line boundary (OCB) normalized convection allows for a quantitative comparison of the convection circulating within the polar cap (interpreted as a result of lobe reconnection, purple) to the Dungey type convection (green).

interactions (e.g., Cowley & Lockwood, 1992; S. E. Haaland et al., 2007; Heppner & Maynard, 1987; Milan, 2015). While the IMF B_z component in the Geocentric Solar Magnetic (GSM) reference frame is found to be the most important single parameter determining the rate of opening of flux on the dayside, the IMF B_y component is found to be crucial in determining how the newly opened flux on the dayside is transported asymmetrically into the nightside lobes, as reflected by large dawn-dusk deflections in the ionospheric convection. These deflections are interpreted to be a consequence of the magnetic tension force acting on newly opened field lines in the dayside magnetopause region (e.g., Cowley, 1981; Khurana et al., 1996; Tenfjord et al., 2015). Since the dayside reconnection line branches into two high-latitude regions of large magnetic shears during IMF B_y conditions (Trattner et al., 2012), the presence of an IMF B_y component leads to oppositely directed dawn-dusk plasma flows on the dayside in the two hemispheres, associated with each of the large shear angle regions on the magnetopause.

Pettigrew et al. (2010) presented climatologies of high-latitude ionospheric convection during each local season. From separate analysis of data from each hemisphere, their results revealed profound differences that depended on the hemisphere, local season, and the sign of the IMF B_y component. One persistent trend they observed was that the convection in the two hemispheres is generally vastly different, even on large scales, since the tilt of Earth's dipole toward/away from the Sun is usually significant ($>10^\circ$ 70% of the time). However, when accounting for both the

dipole tilt effect and the hemispheric differences due to the sign of IMF B_y (for the above-mentioned reasons), the high-latitude convection pattern between the two hemispheres are largely similar. This suggests that dipole tilt and IMF B_y are the most important parameters in introducing global north-south asymmetry of the magnetosphere.

Understanding the cause of the dipole tilt effect on the climatology of global convection (e.g., Pettigrew et al., 2010; Thomas & Shepherd, 2018) is of great scientific interest. It has been pointed out that the lobe reconnection process is likely responsible for hemispheric asymmetries in plasma circulation at polar latitudes, as the lobe reconnection process is not bound by the same north-south symmetry constraints as dayside reconnection, and can hence operate independently in the two hemispheres (e.g., Chisham et al., 2004; Reistad, Laundal, Østgaard, Ohma, Thomas, et al., 2019). This leads to hemispheric differences in the ionospheric flux transport, often quantified by the cross polar cap potential, for example, Pettigrew et al. (2010); Thomas and Shepherd (2018). Distinguishing convection initiated by processes related to the Dungey cycle (which includes both the dayside and nightside reconnection) from convection initiated by lobe reconnection is challenging. This is likely the reason why the lobe reconnection process has mainly been studied when the IMF is mainly northward and the IMF B_y component is relatively small, since under these conditions, the signatures of lobe reconnection can be more readily distinguished from Dungey-type reconnection. However, the question still remains: What is the relative contribution of lobe reconnection to the overall convection pattern when the IMF has a dominant B_y component? The question is important, as the IMF orientation between 1996 and 2019 had $|IMF B_y| > |IMF B_z|$ for 61% of the time (calculated from minute resolution data from NASA's OMNI database), and the dipole tilt angle magnitude $>10^\circ$ for 70% of the time.

The present paper describes an approach for separating the Dungey type convection from the plasma circulation entirely on open field lines, where we attribute the latter to the lobe reconnection processes. This is made possible by simultaneous observations of ionospheric convection and the open/closed field line boundary (OCB). A conceptual illustration of the OCB normalized convection is shown in Figure 1, displaying the global convection features seen in the northern hemisphere during positive IMF B_y conditions in the above mentioned climatological studies. With the knowledge of the high latitude convection relative to the OCB, one can quantify the amount of plasma circulation taking place on open field lines, as illustrated with the purple lobe cell in Figure 1. The quantification of the potential (total magnetic flux transport

rate [$\text{Wb/s} = \text{V}$]) associated with the polar cap plasma circulation, Φ_{lobe} , can be illustrated by the number of closed contours of the electric potential inside the polar cap, and will be described in detail in Section 3. As will be discussed toward the end of the paper, we interpret the polar cap plasma circulation (Φ_{lobe}), as a result of lobe reconnection in a quantitative manner, similar as Reistad, Laundal, Østgaard, Ohma, Thomas, et al. (2019) did for pure northward IMF. The total magnetic flux transport rate is quantified by the cross polar cap potential (potential difference between the global maximum and minimum locations), and will reflect the contribution from all sources, which we assume to be the day- and nightside reconnection processes (Dungey cycle) in addition to lobe reconnection. Hence, the number of contours of the electric potential intersecting the OCB will illustrate the strength of the Dungey cycle, Φ_{Dungey} , represented by the green contours in Figure 1. These quantities relate to the Cross Polar Cap Potential as $\text{CPCP} = \Phi_{\text{Dungey}} + \Phi_{\text{lobe}}$. An inherent assumption for the separation into the two sources is that the ionospheric plasma circulation is a driven process. The method is described in the next section and results are presented in Section 3 and discussed in Section 4. Section 5 conclude the paper.

2. Method

To be able to make quantitative estimates of the lobe reconnection rate during the IMF B_y dominated periods investigated here, the OCB normalization is needed. This section describes the various processing steps involved in producing the convection maps presented in Section 3, with special emphasis on the methodology not described in earlier papers.

2.1. Ionospheric Convection From SuperDARN

We use a database of gridded, line-of-sight (LOS) observations of F-region plasma drift from the Super Dual Auroral Radar Network (SuperDARN) (Chisham et al., 2007; Greenwald et al., 1995). Our database consists of 10^8 individual LOS observations from above 40° magnetic latitude in the northern hemisphere from 2010–2016 CE (Thomas, 2020). This is the same data set used to construct the SuperDARN convection model by Thomas and Shepherd (2018), and is restricted to observations made during standard operating modes. Furthermore, only $\frac{1}{2}$ -hop echoes with slant paths of 800–2,000 km are considered, to optimize accuracy of the geolocation and reduce the influence of low-velocity echoes from the E region. These observations are assumed to originate from an altitude of 300 km. The gridded data set has a spatial resolution of ~ 100 km and a temporal resolution of 2 min (Ruohoniemi & Baker, 1998).

Similar to Newell et al. (2004), we convert the observed LOS velocities to the Sun-fixed magnetic local time/magnetic latitude (MLT/MLAT) frame based on their Altitude Adjusted Corrected GeoMagnetic coordinates (AACGM) (Baker & Wing, 1989) before estimating the average convection (corotation correction). We interpret the ionospheric convection in terms of magnetic flux transport within the magnetosphere, and we argue that the Sun-fixed MLT/MLAT frame is the most appropriate for analyzing these processes. This correction for corotation is done by adding a projection of the eastward corotation velocity to the LOS observation. As pointed out by Newell et al. (2004), the corotation correction causes the dawn cell to increase in size at the expense of the dusk cell, as the corotation component will be along the direction of the return flow at dawn, but opposite to the return flow at dusk. The effects of corotation on the results are further discussed in Section 4.

2.2. Solar Wind and IMF Observations

Simultaneous solar wind and IMF observations are obtained from the 1 min OMNI database (King & Papitashvili, 2005). This data product contains the upstream solar wind conditions time-shifted to the bow shock nose. We have assigned each SuperDARN observation a corresponding solar wind and IMF observation based on an average of a 30 min window, allowing the magnetosphere to respond to the prevailing IMF, and also taking into account the uncertainty in solar wind propagation delay. We use an approach similar to that outlined by S. E. Haaland et al. (2007), and define the window to be from 20 min prior to the OMNI observations to 10 min after. The stability of the IMF in the GSM $Y-Z$ plane in this window is judged by the length of the bias vector, as defined by S. E. Haaland et al. (2007), and we use 0.96 as a threshold to be

consistent with their method. This threshold is in general satisfied $\sim 51\%$ of the time in the solar wind, and efficiently removes intervals of varying IMF orientations.

2.3. Auroral Oval Radius From AMPERE

To scale the convection to the open-closed field line boundary we need simultaneous estimates of this boundary in the northern hemisphere. We use the data set of circle fits to the Region 1/Region 2 (R1/R2) Birkeland current as observed by the Active Magnetosphere and Planetary Electrodynamics Response Experiment (AMPERE) (Milan, 2019). The circle fits have been estimated using a method outlined by Milan et al. (2015) where the sum of the absolute value of the AMPERE Birkeland current density along the circle is minimized by varying the circle radius and center location. This method effectively places the circle between the two bands of R1/R2 currents. When the R1/R2 current system is clearly observed by AMPERE the method is reliable. We use the same criteria to judge the goodness of fit as Milan et al. (2015). This is based on how much the integrated current density along circles of varying radius change, see Figure 1b in Milan et al. (2015). We apply their suggested threshold value of $0.15 \mu\text{A}/\text{m}$, which we find to be fulfilled 85% of the time in the northern hemisphere AMPERE data set from 2010 to 2016.

The reason why we utilize the AMPERE circle fit determined simultaneous to the convection measurements, is to normalize the ionospheric convection to the OCB. However, the R1/R2 circle fit from AMPERE systematically places the boundary equatorward of the OCB. To correct for this, we take into account the typical distance between the OCB and the R1/R2 boundary. Burrell et al. (2020) did a comparison between simultaneous R1/R2 boundaries from AMPERE and OCB boundaries determined from electron precipitation measured by the Defense Meteorological Satellite Program (DMSP) satellites F16–18. They found an average difference of $\sim 3^\circ$, with a slight MLT variation. We employ their MLT-dependent correction as expressed in their equation 1, using the “median coefficients.”

2.4. Scaling Convection to the OCB

When a simultaneous reliable OCB estimate from AMPERE is available, we convert the gridded SuperDARN LOS observations into a new reference frame that is ordered with respect to the OCB and its center location. We use the `ocbpy` Python package (Burrell & Chisham, 2020) to convert each measurement location from AACGM to an OCB-oriented latitude/MLT polar grid, where the pole is the center of the AMPERE circle fit. The location of each measurement is in this way scaled with distance from the inferred OCB location. To do this one must choose a size of the scaled polar cap. We choose an OCB radius of 15° , which is the typical OCB radius during the conditions presented in this analysis. Scaling convection to the OCB has been described earlier by Chisham (2017). They pointed out that for a large versus small polar cap, the same transpolar transport of flux (often referred to as cross polar cap potential) would result in different observed convection electric field. We therefore also scale the convection electric field measurement itself to the simultaneous polar cap size, using Equation 3 in Chisham (2017). This scaling is a built-in feature in the `ocbpy` package used, which also provides the transformed vector components in the OCB frame used in the further analysis.

2.5. Representing the Average Convection Map From the Selected Observations

The analysis presented in this paper is based on the same technique as described in Reistad, Laundal, Østgaard, Ohma, Haaland, et al. (2019); Reistad, Laundal, Østgaard, Ohma, Thomas, et al. (2019) to represent the average convection pattern based on the selection of observations described above using Spherical Elementary Current Systems (SECS) (Amm, 1997; Amm & Viljanen, 1999; Amm et al., 2010). Similar to Reistad, Laundal, Østgaard, Ohma, Thomas, et al. (2019), we use an equal area grid defined along circles of constant latitude with circle spacing of 2° , and a total of 480 grid cells above 60° for the SECS nodes. One improvement relative to the methodology of Reistad, Laundal, Østgaard, Ohma, Thomas, et al. (2019) is that we omit the intermediate step of producing binned averages before representing the convection electric field using SECS. Instead, we perform a direct inversion using the individual (OCB scaled) observations. The SECS representation is found by solving a linear inverse problem of the same form as presented in Reistad, Laundal, Østgaard, Ohma, Thomas, et al. (2019), using damped least squares by applying Tikhonov

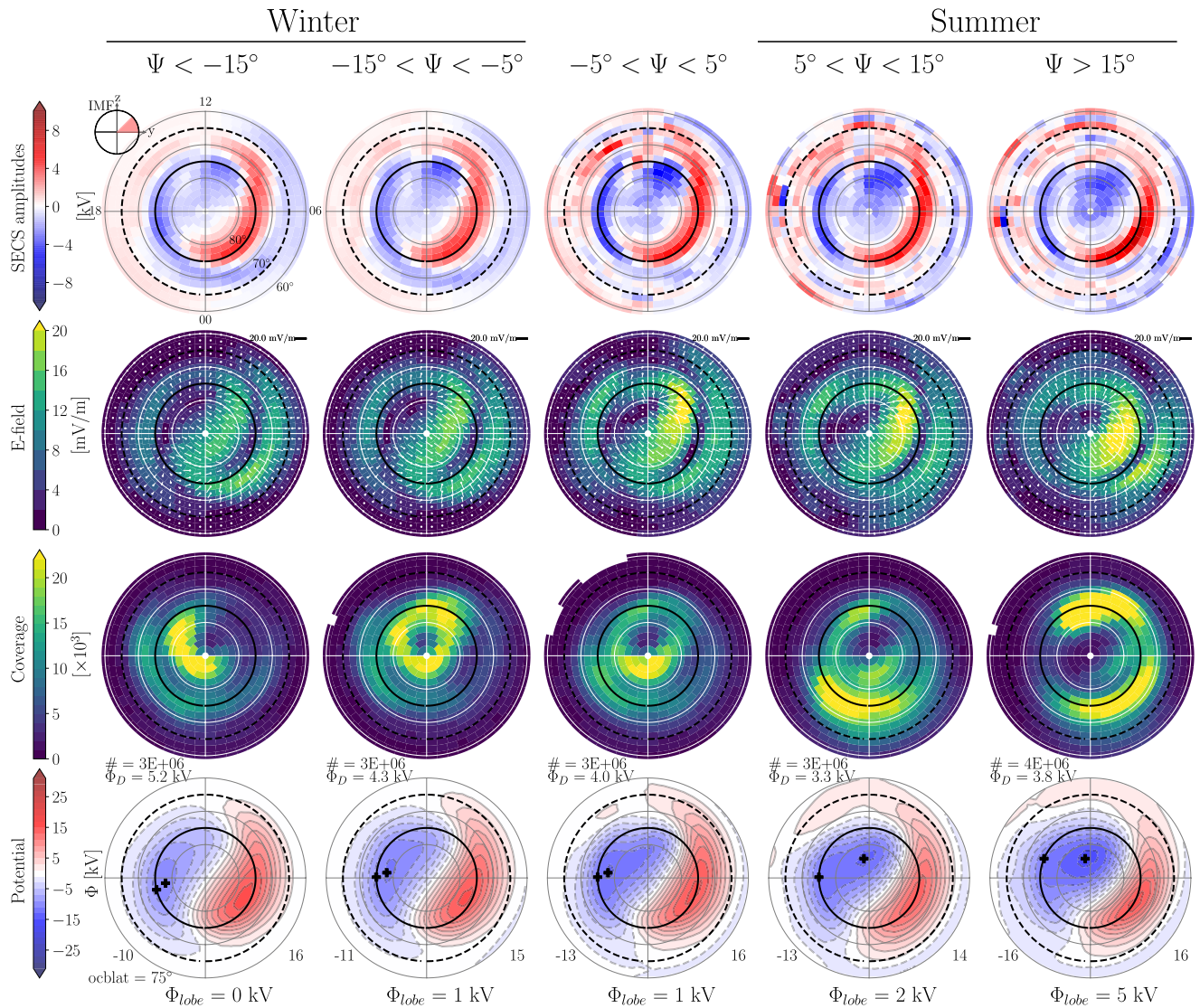


Figure 2. Northern hemisphere convection patterns normalized to the open/closed field line boundary (OCB) when the Interplanetary Magnetic Field (IMF) clock angle θ is in the range $[45^\circ, 90^\circ]$, as also indicated in the small dial inset in the top left corner. Columns: Different intervals of the dipole tilt angle Ψ . Solid black circle in each panel indicate the OCB location to which the convection has been normalized. The imposed $E_{east} = 0$ boundary is shown with a dashed black circle. Top row: Spherical Elementary Current Systems (SECS) amplitudes (what is solved for in the inversion) describing the convection electric field. Second row: Convection electric field described by the SECS representation. Magnitude of \vec{E} in color, vector pins in white. Third row: Coverage shown as number of observations on an equal area grid. Bottom row: Electric potential as described with the SECS amplitudes in the top row. Contour interval is 2 kV. Number of closed contours (in kV) inside the polar cap, Φ_{lobe} , is printed below each panel.

regularization (e.g., Tikhonov et al., 2013). The regularization parameter for each inverse problem is determined through L-curve analysis. The regularization is needed to avoid the problem of over fitting by damping the norm of the solution vector. The challenge with the spherical elementary functions having a singularity at the location of the node is treated as suggested by Vanhamäki and Juusola (2020), namely to redefine the elementary function close to the node. We here use an arc length of half the SECS node separation as the limit of where the function is redefined.

As shown in the third row of Figure 2, the observational coverage changes significantly for the different intervals of the dipole tilt angle. This is a known issue with SuperDARN, and is due to seasonal changes in High Frequency (HF) radio propagation conditions. Seasonal changes in the decameter-scale, ionospheric irregularities that produce the back scattered HF signal combine with the geographic distribution of the radars and the offset of the geomagnetic pole to create a bias in MLT of the radars when sorting by dipole

tilt. To mitigate some of these effects, we weight the observations based on the coverage maps presented in the third row of Figure 2. An even MLT/MLAT weighting is employed by using the weight factor $w = 1/n$ where n is the number of observations in the grid cell that the observation fall within. To avoid placing too much weight on areas of sparse coverage, we place an upper limit of this weight by setting $w_{\max} = 1/n_{\text{lim}}$ when $n < n_{\text{lim}}$. Regions with $n < n_{\text{lim}}$ are filled with white in the third row of Figure 2. In all plots using SuperDARN data we use $n_{\text{lim}} = 100$.

A weak boundary condition of $\vec{E}_{\text{east}} = 0$ at a location 10° equatorward of the OCB is imposed on the solution. This is implemented by adding synthetic observations of zero velocity drift in the northward direction in a ring at this location, with an increased weight compared to the actual observations. Its location is indicated by the dashed black line in Figure 2. This is similar to the Heppner-Maynard boundary used in the map potential fit technique applied to SuperDARN observations (e.g., Shepherd & Ruohoniemi, 2000; Chisham et al., 2007), and is used to ensure that the return flow is confined to a region in vicinity of the auroral zone. Similar zero flow implementations are used in most representations of average ionospheric convection (e.g., Cousins & Shepherd, 2010; Fogg et al., 2020; S. E. Haaland et al., 2007; Heppner & Maynard, 1987).

2.6. Polar Cap Convection From Cluster Electron Drift Instrument-EDI

To test the robustness of the trends of the high latitude normalized convection maps produced from the combined SuperDARN and AMPERE data set, we present an independent convection analysis from measurements originating mainly from the lobes. In this way we can also address our interpretation of the SuperDARN/AMPERE results in terms of a magnetospheric origin, as the magnetospheric observations from the Electron Drift Instrument (EDI) (Paschmann et al., 1997) on board the Cluster spacecraft are simply mapped to the ionosphere using the Tsyganenko 2002 model (Tsyganenko, 2002a, 2002b) assuming equipotential field lines. Hence, the mapped convection presented in Figures 5–7 should not be affected by the local ionospheric conditions in the same way as measurements from SuperDARN, making them a more direct description of the magnetospheric magnetic flux transport.

It has been demonstrated that the EDI mapping technique reproduces the well-known features of the high-latitude convection pattern in both hemispheres (Förster et al., 2015; S. E. Haaland et al., 2007). One further advantage of this data set for our purpose is that the Cluster spacecraft spends large portions of the time of its highly elliptical polar orbit in the magnetotail lobes. Hence, the vast majority of the mapped convection measurements originate above $|80^\circ|$ magnetic latitude, which is ideal for investigating the influence of the lobe reconnection process. On the other hand, the majority of EDI measurements are from the period 2001–2005, during which the OCB was not continuously monitored. Requiring simultaneous OCB estimates would significantly reduce the already sparse number of EDI measurements available for this type of analysis; thus EDI convection measurements are not scaled to the OCB.

It is desirable to examine the influence on the convection pattern by dipole tilt angle Ψ , since Ψ has a large influence on the lobe reconnection process (Crooker & Rich, 1993; Koustov et al., 2017; Reistad, Laundal, Østgaard, Ohma, Thomas, et al., 2019; Wilder et al., 2010; Yakymenko et al., 2018). However, the correlation between Ψ and MLT of the Cluster orbit produces highly uneven sampling of the high latitude regions when Ψ is large. To compensate for this bias, we take advantage of our knowledge of the global coupled two-hemisphere system as well as Cluster's orbit as follows. Cluster has its apogee in the tail around the September equinox, so the intervals of large positive and negative tilt favor observations toward the dawn and dusk flanks, respectively. Since the high latitude electrodynamics in the two hemispheres are known to be largely similar when comparing the same local season (opposite Ψ) under opposite IMF B_y orientations (e.g., Pettigrew et al., 2010), we here combine measurements from the northern and southern lobes in this manner to increase the data coverage. In this way, we obtain sufficient sampling coverage of the combined polar regions during both positive and negative dipole tilt intervals. The weighting and regularization scheme used with the SuperDARN data is also employed for the EDI data analysis. We note that each mapped EDI measurement represent a 2D vector measurement, in contrast to the LOS measurements from SuperDARN. For the EDI analysis, we use $n_{\text{lim}} = 10$ in the weighting scheme. The same weak boundary constraint of $E_{\text{east}} = 0$ is imposed at 60° modified apex magnetic latitude (Richmond, 1995).

The Cluster EDI data were downloaded from the Cluster Science Archive (Laakso et al., 2010), resampled to 1 min resolution and mapped to the ionosphere using the method outlined by S. E. Haaland et al. (2007). For convenience, our approach is summarized in the following paragraph.

The location of Cluster is mapped to 300 km using the Tsyganenko 2002 model. To get the direction of the EDI convection in the ionosphere, a location displaced a distance d from Cluster's location in the direction of the measured convection is also mapped to 300 km. The magnitude of d is set to $50 \text{ km} \cdot \sqrt{B_i/B_m}$, where B_i and B_m are the magnitude of the model magnetic field in the ionosphere and magnetosphere, respectively. With this choice, the mapped positions are always displaced by roughly 50 km in the ionosphere regardless of Cluster's position in the magnetosphere. Finally, the magnitude of the measured convection is scaled by $\sqrt{B_m/B_i}$ to give the corresponding plasma convection at 300 km. To be consistent with the SuperDARN data processing, we apply no correction for corotation as the EDI observations are represented in the GSE (Geocentric Solar Ecliptic) coordinate system prior to mapping.

2.7. Separation on Local Season

Throughout the manuscript, we use the terms dipole tilt (Ψ) and local season (summer/winter) interchangeably. However, all data selection is based on the value of Ψ at the time of observation. Two different geophysical aspects are highly correlated with the dipole tilt angle, and are more accurately quantified using the dipole tilt angle rather than a single scalar representing geographic season (e.g., day of year):

1. The degree of solar illumination of the high magnetic latitude region.
2. Magnetic field geometry at the dayside magnetosphere where IMF interaction takes place (dayside and lobe reconnection).

For the investigations presented here, the latter is likely the most relevant for explaining our results, as will be elaborated on in Section 4. Hence, when referring to a local season (often more convenient as it will make the argument apply to both hemispheres), it will relate to a particular dipole tilt interval, depending on hemisphere, and its implications on the dayside field geometry should be kept in mind. For the SuperDARN analysis from the northern hemisphere, we hence refer to local winter when Ψ is negative, and summer when Ψ is positive. Since we combine hemispheres in the EDI analysis, the particular Ψ interval used when referring to local summer/winter will depend on in which hemisphere the observation originate.

3. Results

3.1. Ionospheric Convection for IMF B_y -Dominated Conditions: SuperDARN Measurements Normalized to OCB

In Figure 2, we show our results of the average convection when the IMF clock angle θ is in the range $[45^\circ, 90^\circ]$. The five columns represent different intervals of the dipole tilt angle Ψ , ranging from local winter conditions in the leftmost column, to local summer in the rightmost column, as all data is from northern hemisphere. In all panels, a solid circle at 75° latitude marks the location of the OCB used to normalize the convection as described in the previous section. The $\bar{E}_{east} = 0$ boundary location is also indicated by a dashed black circle. The top row shows the solution of the inversion described in Section 2.5. In our application, these SECS amplitudes are proportional to $\nabla \cdot \bar{E}$ (Reistad, Laundal, Østgaard, Ohma, Haaland, et al., 2019) and hence also $\nabla \times \bar{v}$, where \bar{E} and \bar{v} are the convection electric field and ionospheric convection field, respectively. Hence, the amplitudes reflect the degree of vorticity in the ionospheric convection. As expected, the largest SECS node amplitudes tend to lie along or near the OCB, reflecting the global two-cell convection pattern which is typically associated with a strong shear (Chisham, 2017; Chisham et al., 2009). Due to the OCB normalization, one can judge to what extent the SECS amplitudes changes inside or outside the polar cap. In Figure 2, we observe a notable increase in SECS node amplitudes within the polar cap with increasing Ψ , suggesting that the source of this increased circulation is on open field lines.

The second row in Figure 2 shows the magnitude of the electric field represented by the SECS amplitudes. We evaluate the electric field on grid points that are between the SECS nodes shown in the upper row, in order to eliminate the singularities close to the nodes. Bin colors and white pins respectively indicate the electric field magnitude and direction. The largest electric field values are typically located in the polar cap.

During local winter, this represents mainly transpolar transport, but for increasing Ψ the polar cap convection becomes stronger and has more directional variations inside the polar cap. We also note the apparently stronger convection electric field in the dawnside return flow region compared to the duskside return flow. As pointed out by Newell et al. (2004), this is expected when the plasma convection is represented in the inertial frame.

The third row shows the data coverage in each Ψ interval. The color represents the number of observations on the same equal area grid as the SECS model is evaluated on (second row). Cells with less than 100 LOS observations are shown as white. For the data selection in Figure 2 this is only the case at latitudes equatorward of the $\vec{E}_{east} = 0$ boundary. We also print the number of individual LOS observations included in the inversion as well as the average dayside reconnection rate during these observations Φ_D using the Milan et al. (2012) coupling function. From these coverage panels it is evident that the spatial coverage is changing with season.

The fourth row shows the electric potential associated with the SECS amplitudes in the top row with a 2 kV contour spacing, evaluated on the same grid as used in the second and third row. As explained by Reistad, Laundal, Østgaard, Ohma, Haaland, et al. (2019), the potential $\Phi(\vec{r})$ is found by summing the potential from each SECS node, which is given by the integral of the SECS curl-free elementary function from the node to \vec{r} . The general two-cell convection pattern is seen, with a round cell at dusk and a crescent cell at dawn due to the positive IMF B_y conditions. The purpose of this study is to estimate the amount of plasma circulation solely within the polar cap associated with the selection conditions. An inherent assumption is that these averages represent a static equilibrium situation during these conditions. Due to the normalization scheme, one can infer the amount of plasma circulating inside the OCB. This measure, we refer to as Φ_{lobe} , and is the minimum potential difference between the min/max potential inside the polar cap for $+B_y/-B_y$, and the potential along the OCB, highlighted by the two black crosses in each potential panel. We interpret Φ_{lobe} as a signature of lobe reconnection in a quantitative manner, and its value is printed below each panel in the bottom row. In addition, the overall minimum and maximum potential values associated with the dusk and dawn cell, respectively, is printed in the lower corners of each panel, and their sum is the cross polar cap potential, here representing the rate of magnetic flux transport from the combined lobe and Dungey cells. Hence, by subtracting Φ_{lobe} from the cross polar cap potential, one gets a measure of the rate of magnetic flux transport across the OCB, quantifying the strength of the Dungey cycle.

Figure 3 shows the results for $\theta \in [-90^\circ, -45^\circ]$ in the same format as Figure 2. Now the tension force on the newly reconnected field lines (both dayside and lobe reconnection) acts in the opposite direction compared to Figure 2, making the high latitude convection pattern vastly different. However, some similar trends are seen as for positive IMF B_y in Figure 2. Specifically, the largest convection electric fields are inside the polar cap, there is primarily transpolar convection in local winter (northern hemisphere), and the convection streamlines are increasingly circular inside the polar cap (potential contours) for increasing Ψ . A seemingly big difference between the electric potential contours in Figures 2 and 3 is the apparent size of the dawn convection cell. Since lobe reconnection leads to circulation in the same direction as the dusk cell for positive IMF B_y , the dusk cell increases in magnitude for increased lobe reconnection for positive IMF B_y . This is what we see in Figure 2, where the dusk cell is weaker in magnitude than the dawn cell when $\Psi \leq -15^\circ$ but of similar magnitude when $\Psi \geq 15^\circ$. The opposite effect is seen in Figure 3 where IMF B_y is negative. Here lobe reconnection enhances the dawn convection cell, making it increase in strength. In addition, in Figure 3 the dusk cell is seen to reduce in strength for increasing Ψ , while the dawn cell at the same time grows more than the increased circulation inside the polar cap.

To investigate the influence of lobe reconnection when the IMF is purely in the east-west direction, we show the same analysis for the IMF clock angle interval $|\theta| \in [80^\circ, 100^\circ]$ in Figure 4. In general, the ionospheric convection pattern is stronger compared to Figures 2 and 3 since increased θ leads to increased Φ_D . For the positive IMF B_y interval (top row in Figure 4) there is relatively little lobe circulation inside the polar cap, only 3 kV, compared to 5 kV when $\theta \in [45^\circ, 90^\circ]$. For negative IMF B_y , slightly stronger polar cap circulation is also seen for the pure B_y interval in the bottom row in Figure 4, indicating 6 kV, compared to 7 kV in Figure 3. Similar to Figures 2 and 3, Figure 4 also shows that for increasing Ψ , the convection inside the polar cap becomes more circular compared to the pure transpolar convection seen when $\Psi < -15^\circ$.

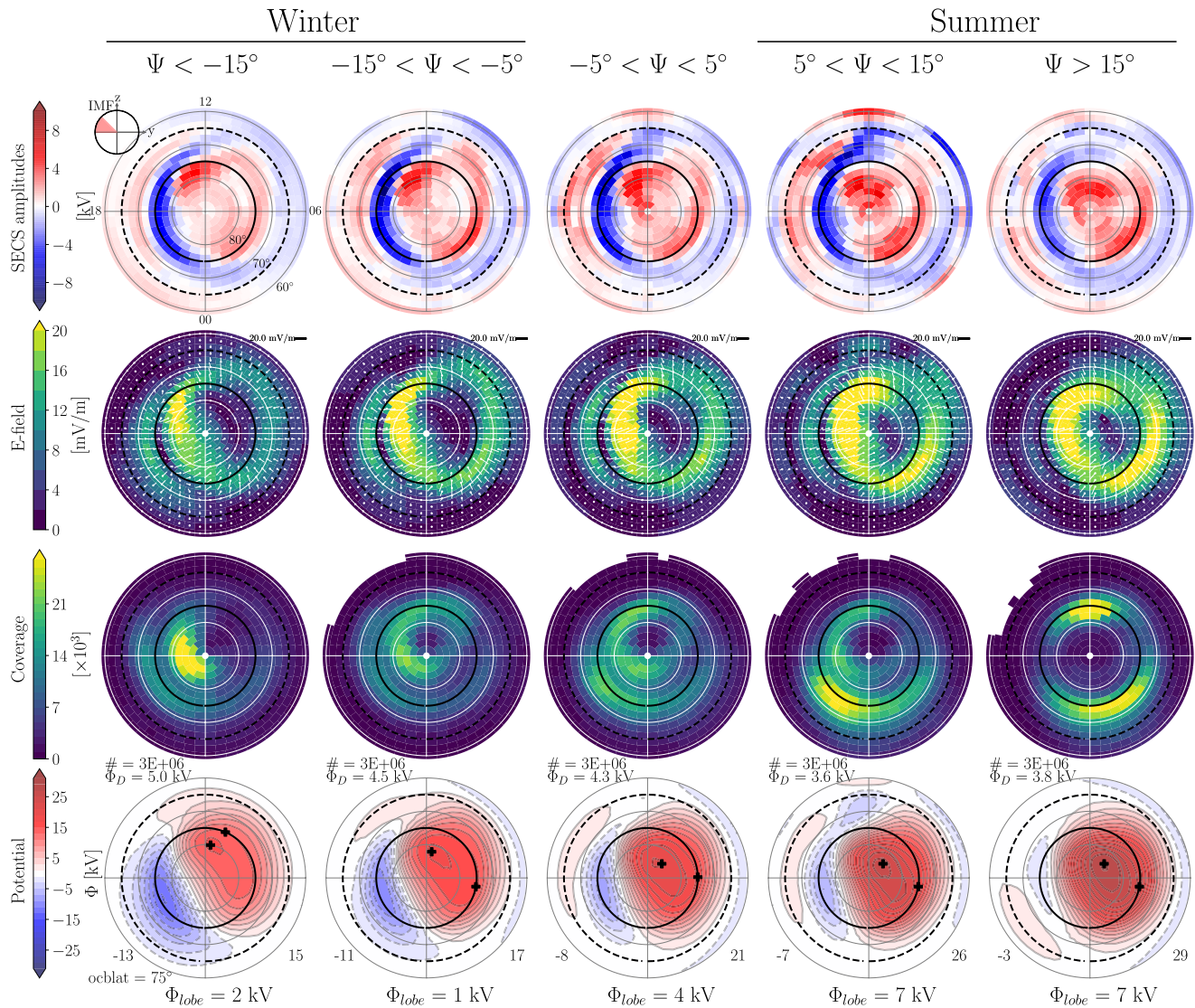


Figure 3. The same format as Figure 2, but for $\theta \in [-90^\circ, -45^\circ]$.

3.2. Ionospheric Convection During IMF B_y Conditions: Results From Mapped Cluster EDI Observations

As an independent test of the trends reported above, we also show analysis of an independent data set to address the significance of the very different ionospheric convection seen in the polar cap for negative versus positive Ψ conditions during IMF B_y periods. As pointed out in Section 2.6, the EDI data coverage does not allow the same strict criteria on Ψ as used with SuperDARN. Therefore, the local seasons are here based on data when $|\Psi| > 5^\circ$ and combining hemispheres as described in Section 2.6. The comparison with the mapped EDI results is highly relevant, as these measurements are not affected in the same way by the magnetosphere-ionosphere coupling. The magnetospheric convection measurements are simply mapped along the magnetic field lines, assuming no potential drop along the field. Figures 5–7 show the results of the mapped Cluster EDI data set in the same format as Figures 2–4. We have combined the two hemisphere and this “pairing” is indicated in the IMF dial inset with letters “N” and “S.” Regions with less than 10 observations per grid cell are filled with white. The EDI data set is suited for this investigation as the majority of its measurements originate from the magnetotail lobes, as is evident in the coverage panels in Figures 5 and 6. Although a similar scaling to the OCB is not possible for this data set due to the sparsity of both observations and reliable global estimates of the OCB, the trends at high latitudes can still be compared to the normalized

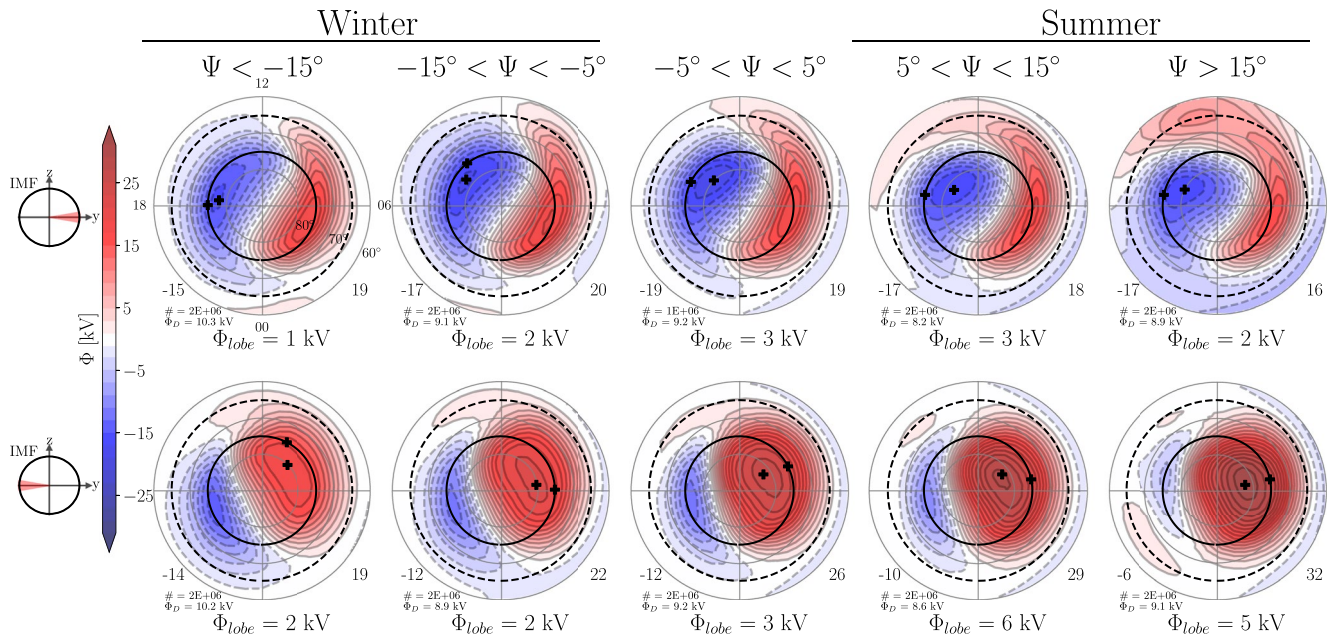


Figure 4. Maps of electric potential on the same format as bottom panel in Figure 2, but for $\theta \in [80^\circ, 100^\circ]$ in the top row and $\theta \in [-100^\circ, -80^\circ]$ in the bottom row. Contour interval is 2 kV.

maps in Figures 2–4. To aid this comparison, we have indicated a likely location of the average OCB in the Cluster EDI maps presented in Figures 5–7 as a circle that follow the potential ridge on the crescent convection cell. Similar to the SuperDARN analysis, we have applied the same zero electric field constraint to the SECS inversion 10° equatorward of this assumed average OCB location. Although these estimated Φ_{lobe} values from the mapped EDI measurements should not be directly compared to the SuperDARN analysis above, since a normalization is not performed, the increase in Φ_{lobe} from local winter to local summer is in qualitative agreement with the normalized SuperDARN convection maps.

Differences and similarities between the EDI and SuperDARN derived convection maps will be discussed further in the next section.

4. Discussion

4.1. Interpretation in Terms of Lobe Reconnection Rate

Quantitative estimates of the contribution from lobe reconnection to high-latitude plasma convection are presently lacking in our system-level description of IMF B_y dominated periods. This study was designed to target this gap in knowledge by developing methods that allow for quantitative estimates of the average ionospheric plasma circulation solely within the polar cap when IMF B_y dominates. We largely build on previous work (Reistad, Laundal, Østgaard, Ohma, Haaland, et al., 2019; Reistad, Laundal, Østgaard, Ohma, Thomas, et al., 2019) that used the same SECS representation of the ionospheric convection as presented here. Reistad, Laundal, Østgaard, Ohma, Thomas, et al. (2019), who focused on pure northward IMF intervals, argued that the strong coupling between the polar ionosphere and the magnetosphere makes the high latitude ionospheric convection to first order reflect the forcing from the magnetosphere. Under this assumption, the ionospheric plasma circulation solely within the polar cap seen in Figures 2–4 reflects its magnetospheric origin. This interpretation is supported by the EDI measurements of plasma convection mainly from the lobes and high altitude polar cap regions showing a similar plasma circulation (Figures 5–7). This type of magnetospheric lobe circulation was also seen by S. Haaland et al. (2008) during IMF B_y dominated periods in the Cluster EDI data, without mapping the measurements to the ionosphere. This behavior is expected from the lobe reconnection process, and is often referred to as stirring of lobe flux (e.g., Milan et al., 2020; Reiff & Burch, 1985). In the following discussion we interpret our quantified measure of

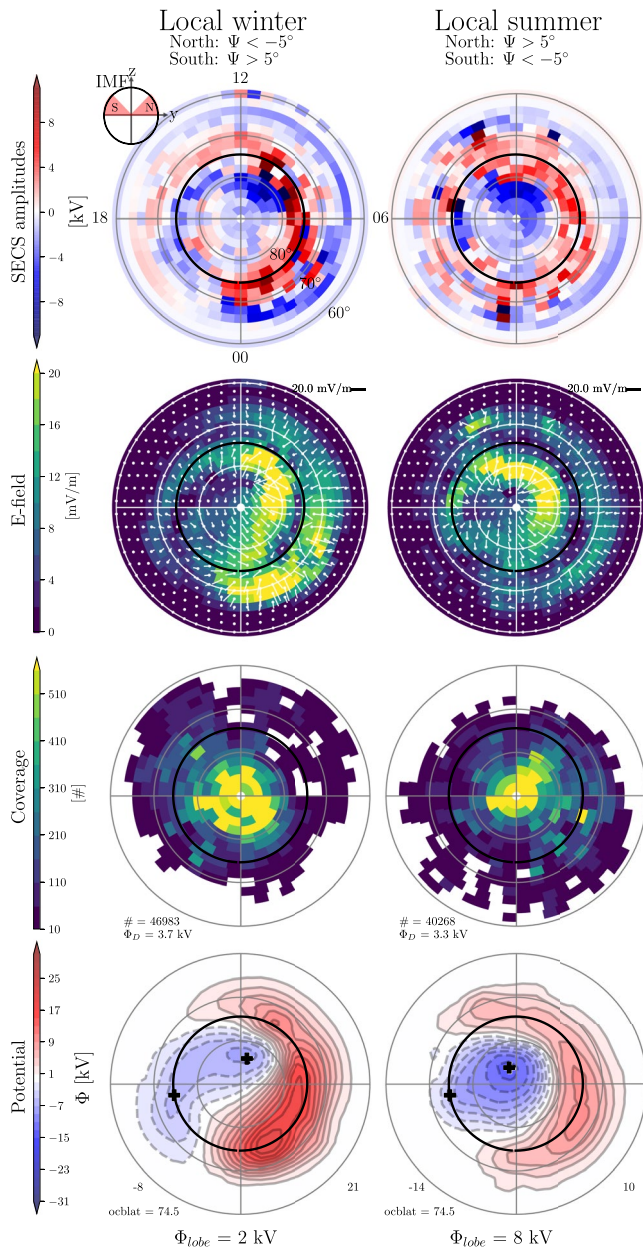


Figure 5. Analysis of the Cluster Electron Drift Instrument (EDI) data, mapped to the ionosphere. No normalization to the open/closed field line boundary (OCB) is done here; the black circle that follows the ridge of the crescent convection cell is here only shown for reference. The processing and the format of this figure is identical to Figure 2. As indicated in the top title and clock angle dial, we here combine data from both hemispheres when they are exposed to similar local Interplanetary Magnetic Field (IMF) B_y and dipole tilt forcing.

plasma circulation within the polar cap, Φ_{lobe} , as an estimate of an average lobe reconnection rate associated with the data selection conditions.

An important result from the presented OCB normalized convection maps is that significant Φ_{lobe} is seen when IMF B_y dominates. This highlights that lobe reconnection likely plays an important role in high latitude electrodynamics when IMF B_y is dominant. When IMF $B_z \sim 0$, Figure 4 indicates that Φ_{lobe} is slightly smaller than when the absolute value of the IMF clock angle, $|\theta| \sim 70^\circ$; Φ_{lobe} nevertheless lies in the range 3–6 kV on average during local summer conditions. This finding stands somewhat in contrast to the lobe reconnection coupling parameter $E_{RC} = V B_T \cos^4(|\theta|)$ proposed by Wilder et al. (2008), which is designed to favor northward IMF and approach 0 as θ approaches $\pm 90^\circ$. This coupling parameter expresses an electric field associated with the reversed convection seen during northward IMF, and is intended to represent the lobe reconnection electric field. Here V and B_T denote the solar wind velocity and transverse component of the IMF, respectively. The large exponent causes the value of E_{RC} to rapidly approach 0 with increasing $|\theta|$, in contrast to results presented in the previous section. Comparing the lobe reconnection rate inferred during pure northward IMF by Reistad, Laundal, Østgaard, Ohma, Thomas, et al. (2019) (4 kV in winter, 8 kV in summer) to the lobe reconnection rate during the IMF B_y intervals considered here, it appears that that the Wilder et al. (2008) coupling parameter is not applicable when $|\text{IMF } B_y| \gtrsim |\text{IMF } B_z|$. However, we note that the Wilder et al. (2008) coupling parameter (E-field [V/m]) is not directly comparable to the lobe reconnection rate which we address here (rate of magnetic flux transport inside the polar cap [$\text{Wb/s} = \text{V}$]) as the length of the lobe reconnection x-line may vary with IMF clock angle. Although the effect of lobe reconnection during IMF B_y periods has not been quantified on an average basis earlier, its qualitative influence has been suggested by, for example, Crooker and Rich (1993); Frey et al. (2004); Nishida et al. (1998); Reiff and Burch (1985); Sandholt et al. (1998).

4.2. Hemispheric Differences in Asymmetric IMF B_y Forcing Due to Dipole Tilt

When discussing high latitude convection cells during IMF B_y periods, the dawn and dusk convection cells are often referred to as “round” and “crescent.” We also use this terminology to avoid repeating both the sign of IMF B_y and the hemisphere under consideration.

Another feature evident in both the OCB normalized and to some extent the mapped EDI convection maps, is that the round convection cell is distinctively more circular during local summer than during local winter. This can be seen, especially in Figures 2–4, where the ionospheric convection is mainly across the polar cap in local winter. Since the convection has been normalized to the OCB (black circle), we can here determine that the turning of the convection flow on the round cell on the dayside from return flow (sunward) into transpolar flow (anti-sunward) takes place outside the OCB for $\Psi < -15^\circ$. For increasing values of Ψ , this transition takes place more and more inside the OCB. This is different from the crescent cell that looks similar in shape on the dayside regardless of season, with largest shear near the OCB. We suggest that this seasonal behavior of the dayside polar cap flow with IMF B_y is the same effect as reported by Milan et al. (2001), observing similar seasonal IMF B_y signatures of the dayside ionospheric convection between $76^\circ - 81^\circ$ MLAT from a single beam of the CUTLASS radar. Our results provide more context, as we present an average of the

transition takes place more and more inside the OCB. This is different from the crescent cell that looks similar in shape on the dayside regardless of season, with largest shear near the OCB. We suggest that this seasonal behavior of the dayside polar cap flow with IMF B_y is the same effect as reported by Milan et al. (2001), observing similar seasonal IMF B_y signatures of the dayside ionospheric convection between $76^\circ - 81^\circ$ MLAT from a single beam of the CUTLASS radar. Our results provide more context, as we present an average of the

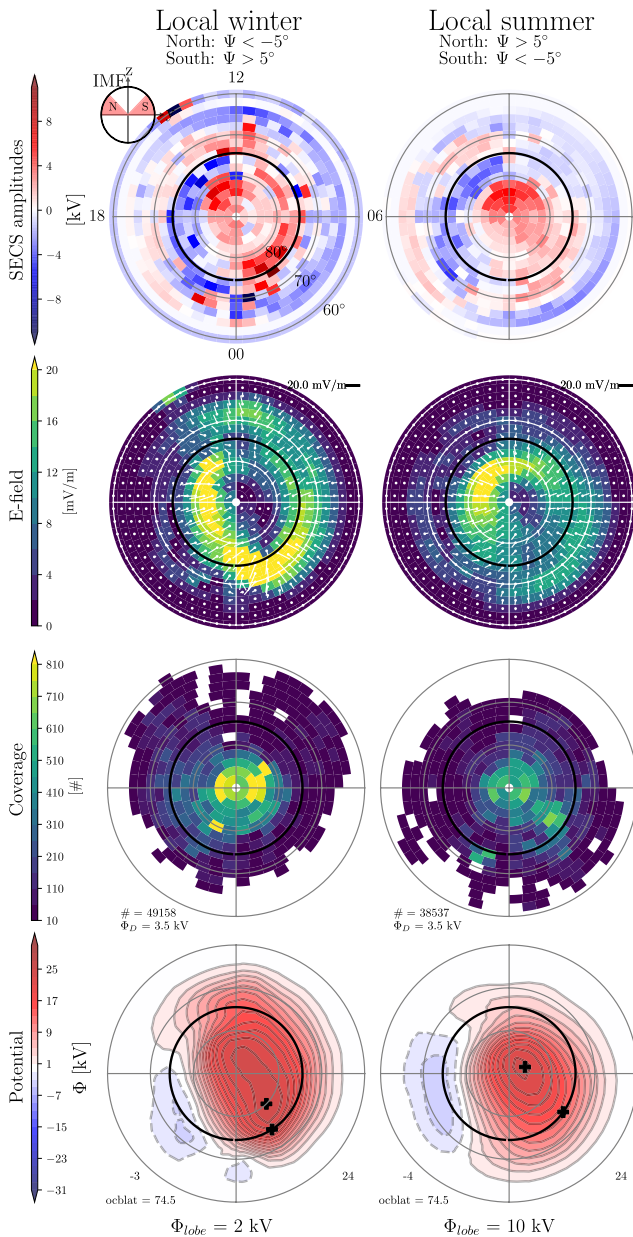


Figure 6. Same as Figure 5 but for the opposite Interplanetary Magnetic Field (IMF) B_y direction as indicated with the clock angle dial.

entire high latitude region, and also normalize the convection to the OCB. Nevertheless, our interpretation is similar to that of Milan et al. (2001) in the sense that we attribute the strong east/west flows on the round cell to the tension force acting on the newly reconnected field lines (both merging with closed and open field lines). The seasonal differences suggest that the tension force transmitted to the winter and summer ionospheres is very different. For example, if the dayside reconnection takes place at a distance away from the subsolar region toward higher latitudes as the maximum shear model suggests (Trattner et al., 2012), the tension on the winter hemisphere footprint of the newly opened field lines will have a less direct influence compared to the summer hemisphere.

This interpretation has implications for how we describe IMF B_y forcing of the magnetosphere-ionosphere system (Khurana et al., 1996; Ohma et al., 2018; Østgaard et al., 2018; Reistad et al., 2016; Tenfjord et al., 2015, 2018). A B_y component is induced in the magnetosphere in response to IMF B_y due to how the tension on newly reconnected field lines (from both dayside and lobe reconnection) lead to asymmetric magnetic flux distributions in the lobes in the two hemispheres. If the two hemispheres are forced differently in this regard (tension force has less direct influence in winter hemisphere end, and lobe reconnection is mainly in summer hemisphere), as our results suggest, the asymmetric IMF forcing will be different in the two lobes. Our results suggest that the summer hemisphere is more prone to the asymmetric addition of flux, while flux is more symmetrically added into the winter hemisphere. In addition, since the lobe reconnection process is more efficient in the summer hemisphere, as also numerous earlier studies have suggested (e.g., Crooker & Rich, 1993; Frey et al., 2004; Koustov et al., 2017; Reistad, Laundal, Østgaard, Ohma, Thomas, et al., 2019), this will add to the north/south asymmetry of the tension forces mentioned above, and also contribute to an asymmetric redistribution of flux, mainly within the summer hemisphere lobe. Hence, we suggest that the combination of the north/south differences in tension force and the north/south differences in lobe reconnection rate leads to the large observed differences in the polar ionospheric convection patterns for positive versus negative dipole tilt conditions. This implies that during intervals of significant dipole tilt and IMF B_y (which is the typical situation), one hemisphere will experience more asymmetric forcing of the lobes than the other. This asymmetric asymmetry situation is common, and will affect the closed field line region differently in the two hemispheres.

4.3. Comparison of Normalized SuperDARN and EDI Convection Maps

Although the same OCB normalization was not possible for the EDI analysis, the results show a number of trends consistent with the normalized convection from SuperDARN, some of which was pointed out above. The more circular convection pattern on the round convection cell during local summer compared to local winter is seen also in the EDI analysis for both IMF B_y directions, see, for example, Figure 7. However, the lobe reconnection rate cannot be directly quantified without the OCB normalization scheme. In Figures 5–7, we have drawn a circle at 74.5° MLAT, which is close to the ridge of the electric potential on the crescent cell, to suggest a possible location of the average OCB. However, as the measurements are not normalized to such a boundary, we put more emphasis on Φ_{lobe} inferred from the SuperDARN analysis. It is therefore questionable whether the strong Φ_{lobe} seen in Figure 7 actually reflects the lobe reconnection rate during these conditions as the corresponding analysis based on OCB normalized data in Figure 4 has more moderate values. We also point out that the OCB frame

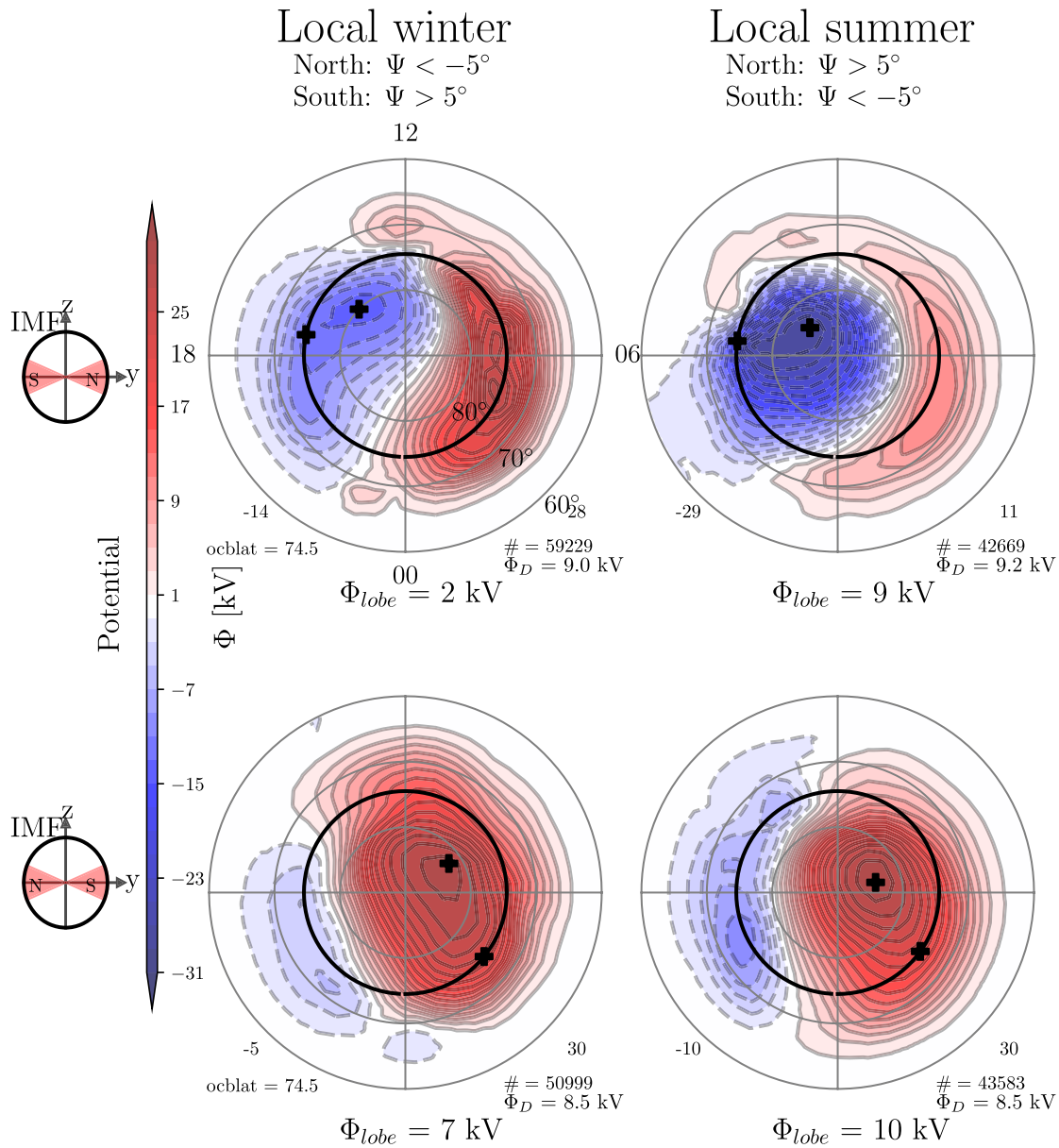


Figure 7. Maps of electric potential in the same format as bottom panel in Figure 5. The two rows combine Interplanetary Magnetic Field (IMF) B_y directions in the two hemispheres in the two possible ways (that will not average out the IMF B_y forcing), as indicated with the clock angle dial. Contour interval is 2 kV.

is on average shifted toward the nightside, making the circle centered at the magnetic pole in Figures 5–7 less accurate for representing an average OCB at all MLTs.

The processing steps involved in both analyses shown here are prone to uncertainties from each of the multiple steps involved. Uncertainties related to variations in the underlying data has been investigated using bootstrap re-sampling (e.g., Efron & Tibshirani, 1994). We have drawn 50 bootstrap samples (of the same size as number of data points, drawn with replacement) for each θ and Ψ interval to repeat the above described analysis using the same regularization parameter, but updating the weighting based on the re-sampled coverage. The results of the 50 different model realizations produced very similar results for the SuperDARN analysis. This is likely related to the large number of observations (typically several millions individual LOS measurements) resulting in a well defined average convection pattern in each sample. The standard deviation of the estimated cross polar cap potentials and Φ_{lobe} from analysis of the 50 different bootstrap samples are all in the range 0.01–0.13 kV. However, this uncertainty only reflects the underlying variability of the

data, describing how well an average convection pattern is determined using the normalization and inversion scheme described. Any additional biases and uncertainty that may have been introduced as part of our normalization and inversion scheme are not captured by this metric. For the EDI analysis, the bootstrap variations are in the range 0.4–3.1 kV for the cross polar cap potential. We encourage the community to test these results with independent data and model analysis to better understand the quantitative impact of the lobe reconnection process on the high latitude electrodynamics. The possible contribution from viscous-like interactions at the magnetopause would be interesting to investigate, but to separate this effect is outside the scope of the present work.

There are also features in the presented convection maps that we are not able to explain. One is the decrease of the dusk cell magnitude with increasing dipole tilt in the SuperDARN analysis during negative IMF B_y , as seen in Figures 3 and 4. Although the Dungey type potential shows consistent values across seasons (shown in the next subsection), the relative strengths of the dawn and dusk cells are not as expected when comparing summer and winter. During positive IMF B_y , this does not seem to be an issue. It has been pointed out that ionospheric plasma convection in darkness is in general more structured than when sunlit (e.g., Cumnock et al., 1995). Due to the spatial resolution of the SuperDARN measurements and the global averaging approach we have applied to the data, any local ionospheric differences (such as the structuring mentioned above) may have an impact on the results that makes the interpretation in terms of a magnetospheric source challenging when comparing sunlit versus dark ionospheres. The trends seen in SuperDARN regarding the relative size of the dawn and dusk cell for \pm IMF B_y are not evident in the EDI analysis, which may not be affected by the local ionospheric conditions in the same way. The EDI results show an opposite trend, if any, in the size of the dusk cell during negative IMF B_y for winter versus summer.

As mentioned in Section 2, the relative size of the dawn and dusk cell is affected by the co-rotation correction. Since we want to interpret the ionospheric convection in terms of flux-transport in a Sun-fixed magnetosphere, we argue that the most relevant frame to analyze this process is the Sun-fixed MLT/MLAT coordinate system as shown here. This choice of reference frame also has some influence on the circulation seen inside the polar cap, Φ_{lobe} . If we do not correct for co-rotation in the SuperDARN analysis, we observe stronger Φ_{lobe} for positive IMF B_y (8 kV for $\Psi > 15^\circ$, $\theta \in [45^\circ, 90^\circ]$) and weaker Φ_{lobe} for negative IMF B_y (3 kV for $\Psi > 15^\circ$, $\theta \in [-90^\circ, -45^\circ]$), compared to the results presented in Figures 2 and 3. However, the influence from the choice of reference frame should not be very different for the different dipole tilt intervals studied.

Despite the challenges mentioned, the trends we see with a significantly rounder convection cell in local summer versus local winter is a feature persistent throughout our entire analysis (SuperDARN and EDI) and not sensitive to the many assumptions made in this analysis.

4.4. Comparison of Dungey and Lobe Convection

It is debated whether the dipole tilt can significantly modulate the dayside reconnection rate (e.g., Cliver et al., 2000; Lockwood et al., 2020). In any case, its effect on Dungey type convection must be the same in both hemispheres. Therefore, the Dungey type potential should be comparable between intervals of the same absolute dipole tilt angle, that is, comparing columns 1 and 5 and column 2 and 4 in Figures 2–4. We define the Dungey potential Φ_{Dungey} as the maximum potential difference across the entire map (cross polar cap potential) minus the contribution from polar cap circulation, Φ_{lobe} . In Figure 8a, we show Φ_{Dungey} for the four different IMF clock angle (θ) intervals presented in this study, from the SuperDARN analysis only. No severe differences in Φ_{Dungey} are seen across season. Furthermore, comparing positive and negative dipole tilt intervals, Φ_{Dungey} is similar within 4 kV during the same θ interval. These differences are typically smaller than the corresponding values deduced from the cross polar potential reported by E. G. Thomas and Shepherd (2018) in their Table 2 for similar IMF and season selections. We suggest that the small variations in Φ_{Dungey} reported here is due to the subtraction of the plasma circulation associated with the lobe reconnection process. We also note that for the $80^\circ < |\theta| < 100^\circ$ conditions, opposite signs of IMF B_y and dipole tilt show a slight asymmetry, suggesting slightly elevated values of Φ_{Dungey} when Ψ and IMF B_y has opposite signs. These are the same conditions that have recently been shown to be associated with enhancements in the westward electrojets (Holappa & Mursula, 2018), radius of the R1/R2 current system (Reistad et al., 2020), energetic electron precipitation (Holappa et al., 2020), and substorm onset frequency (Ohma et al., 2021). Our inferred Φ_{Dungey} when $80^\circ < |\theta| < 100^\circ$ hence supports that the previous mentioned

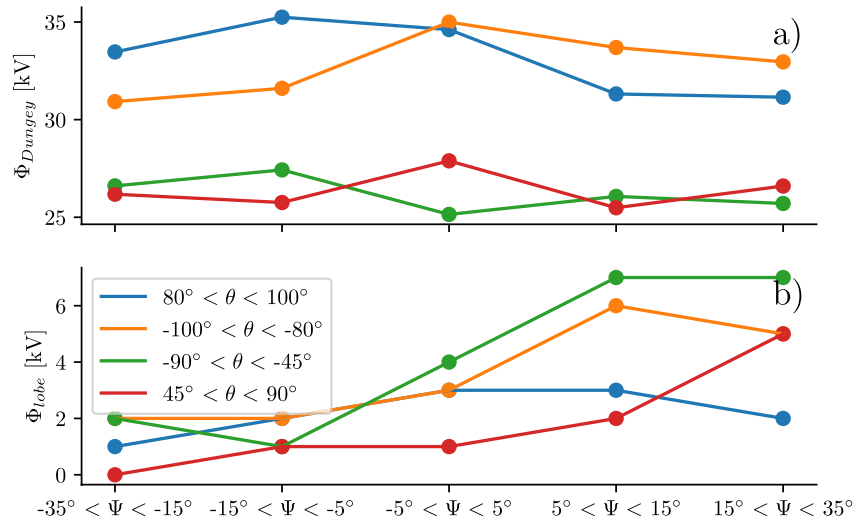


Figure 8. (a) Dungey type potential Φ_{Dungey} estimated from the SuperDARN analysis for the four different Interplanetary Magnetic Field (IMF) clock angle intervals, θ . We define Φ_{Dungey} as the total potential difference across the high latitudes, minus Φ_{lobe} . The x-axis corresponds to the different intervals of the dipole tilt angle. (b) Φ_{lobe} (inferred lobe reconnection rate) on the same format as the above panel.

asymmetries (Holappa & Mursula, 2018; Ohma et al., 2021; Reistad et al., 2020) can be explained by the dayside reconnection rate being affected by the combination of dipole tilt and IMF B_y (Ohma et al., 2021; Reistad et al., 2020). However, further investigations are needed to confirm this.

For completeness, Figure 8b show Φ_{lobe} in the same format as the upper panel, summarizing Figures 2–4, indicating larger values of Φ_{lobe} during negative versus positive IMF B_y . We also note that the bootstrap uncertainties described in the above paragraph are not visible on the scale in Figure 8. As a quantitative estimate of the overall importance of lobe reconnection compared to the Dungey cycle during IMF B_y dominated periods in local summer, we compute the ratio $\langle \Phi_{lobe} \rangle / \langle \Phi_{Dungey} \rangle$. Considering all four θ intervals during the two largest Ψ intervals in Figure 8, this ratio is 16%. Furthermore, this ratio is larger for the $|\theta| \in [45^\circ, 90^\circ]$ intervals (20%) compared to the $|\theta| \in [80^\circ, 100^\circ]$ intervals (12%).

5. Conclusions

Although quantifying the average plasma circulation inside the polar cap when $|IMF B_y| > |IMF B_z|$ is challenging, we believe we have developed a method that takes into account the various factors that are important for the final results. The results presented in Section 3.1 of the OCB normalized average ionospheric convection is, to our knowledge, the first observational attempt to do so. Our main conclusions regarding the ionospheric convection during IMF B_y dominated periods can be summarized as follows:

1. During local winter (as defined by the dipole tilt angle), the transition from return flow to anti-sunward flow takes place equatorward of, or close to, the dayside OCB. In summer, this transition takes place largely inside the polar cap on the round convection cell. This suggests that the tension force from the newly opened field lines has a more direct influence in the local summer hemisphere, causing the summer hemisphere to experience more asymmetric loading of flux compared to the simultaneous flux loading in the winter hemisphere.
2. A consequence of (1) is that the closed magnetosphere will experience asymmetric forcing from the lobes differently in the two hemispheres. Since the magnetosphere often experience a dipole tilt and IMF B_y , this asymmetric asymmetry state of the magnetosphere is common.
3. We have quantified the magnetic flux circulation inside the polar cap, Φ_{lobe} , and suggest this can be a proxy for the lobe reconnection rate. We find that during local summer and IMF B_y dominated conditions ($|\theta| \in [45^\circ, 90^\circ]$), Φ_{lobe} can typically be $\sim 20\%$ of the flux transport associated with the Dungey cycle.

This is different from the local winter conditions, where the contribution from lobe reconnection is found to be almost absent (0–2 kV).

- For the IMF clock angles ($|\theta| \in [45^\circ, 90^\circ]$), we suggest that the lobe reconnection rate is typically 5–7 kV in local summer and 0–2 kV in local winter.

Data Availability Statement

The SuperDARN data set is available at <https://doi.org/10.5281/zenodo.3618607>. Cluster EDI data are available from the Cluster Science Archive: <https://www.cosmos.esa.int/web/csa>. The authors acknowledge the use of NASA/GSFC Space Physics Data Facility (<http://omniweb.gsfc.nasa.gov>) for OMNI data, and the AMPERE radius data set available at https://leicester.figshare.com/articles/dataset/AMPERE_R1_R2_FAC_radii/11294861/1. They also thank the authors of the software packages `secsy`, `ocbpy`, and `dipole` (found on [GitHub.com](https://github.com) with the same name, used for SECS implementation, OCB normalization, and dipole tilt angle calculation, respectively), and the Tsyganenko magnetic field model (<https://geo.phys.spbu.ru/~tsyganenko/modeling.html>). The analysis code may be shared upon request.

Acknowledgments

The authors acknowledge the use of SuperDARN data. SuperDARN is a collection of radars funded by the national scientific funding agencies of Australia, Canada, China, France, Italy, Japan, Norway, South Africa, UK, and United States. J. P. Reistad and K. M. Laundal were funded by the Norwegian Research Council (NRC) through grant 300844/F50. K. M. Laundal and S. M. Hatch were funded by the Trond Mohn Foundation. S. Haaland and A. Ohma was supported by the NRC under grant 223252. A. G. Burrell was funded by the Office of Naval Research. E. G. Thomas thanks the National Science Foundation for support under grant AGS-1934997. The project was also supported by the NRC under grant 223252.

References

- Amm, O. (1997). Ionospheric elementary current systems in spherical coordinates and their application. *Earth Planets and Space*, 49(7), 947–955. <https://doi.org/10.5636/jgg.49.947>
- Amm, O., Grocott, A., Lester, M., & Yeoman, T. K. (2010). Local determination of ionospheric plasma convection from coherent scatter radar data using the SECS technique. *Journal of Geophysical Research*, 115(A3). <https://doi.org/10.1029/2009JA014832>
- Amm, O., & Viljanen, A. (1999). Ionospheric disturbance magnetic field continuation from the ground to the ionosphere using spherical elementary current systems. *Earth Planets and Space*, 51, 431–440. <https://doi.org/10.1186/BF03352247>
- Baker, K. B., & Wing, S. (1989). A new magnetic coordinate system for conjugate studies at high latitudes. *Journal of Geophysical Research*, 94(A7), 9139. <https://doi.org/10.1029/JA094iA07p09139>
- Burrell, A., & Chisham, G. (2020). *aburrell/ocbpy: Version 0.2.1*. Zenodo. <https://doi.org/10.5281/zenodo.4289226>
- Burrell, A. G., Chisham, G., Milan, S. E., Kilcommons, L., Chen, Y. J., Thomas, E. G., & Anderson, B. (2020). AMPERE polar cap boundaries. *Annales Geophysicae*, 38(2), 481–490. <https://doi.org/10.5194/angeo-38-481-2020>
- Chisham, G. (2017). A new methodology for the development of high-latitude ionospheric climatologies and empirical models. *Journal of Geophysical Research: Space Physics*, 122(1), 932–947. <https://doi.org/10.1002/2016JA023235>
- Chisham, G., Freeman, M. P., Abel, G. a., Bristow, W. a., Marchaudon, a., Ruohoniemi, J. M., & Sofko, G. J. (2009). Spatial distribution of average vorticity in the high-latitude ionosphere and its variation with interplanetary magnetic field direction and season. *Journal of Geophysical Research*, 114(9). <https://doi.org/10.1029/2009JA014263>
- Chisham, G., Freeman, M. P., Coleman, I. J., Pinnock, M., Hairston, M. R., Lester, M., & Sofko, G. (2004). Measuring the dayside reconnection rate during an interval of due northward interplanetary magnetic field. *Annales Geophysicae*, 22(12), 4243–4258. <https://doi.org/10.5194/angeo-22-4243-2004>
- Chisham, G., Lester, M., Milan, S. E., Freeman, M. P., Bristow, W. A., Grocott, A., et al. (2007). A decade of the Super Dual Auroral Radar Network (SuperDARN): Scientific achievements, new techniques and future directions. *Surveys in Geophysics*, 28, 33–109. <https://doi.org/10.1007/s10712-007-9017-8>
- Cliver, E. W., Kamide, Y., & Ling, A. G. (2000). Mountains versus valleys: Semiannual variation of geomagnetic activity. *Journal of Geophysical Research*, 105, 2413–2424. <https://doi.org/10.1029/1999JA900439>
- Cousins, E. D. P., & Shepherd, S. G. (2010). A dynamical model of high-latitude convection derived from SuperDARN plasma drift measurements. *Journal of Geophysical Research*, 115. <https://doi.org/10.1029/2010JA016017>
- Cowley, S. W. H. (1981). Magnetospheric asymmetries associated with the y-component of the IMF. *Planetary and Space Science*, 29, 79–96. [https://doi.org/10.1016/0032-0633\(81\)90141-0](https://doi.org/10.1016/0032-0633(81)90141-0)
- Cowley, S. W. H., & Lockwood, M. (1992). Excitation and decay of solar wind-driven flows in the magnetosphere-ionosphere system. *Annales Geophysicae*, 10(1–2), 103–115.
- Crooker, N. U., & Rich, F. J. (1993). Lobe cell convection as a summer phenomenon. *Journal of Geophysical Research*, 98(A8), 13403–13407. <https://doi.org/10.1029/93JA01037>
- Cumnock, J., Heelis, R., Hairston, M., & Newell, P. (1995). High-latitude ionospheric convection pattern during steady northward interplanetary magnetic field. *Journal of Geophysical Research*, 100(A8), 14537–14555. <https://doi.org/10.1029/94ja03318>
- Efron, B., & Tibshirani, R. J. (1994). *An introduction to the bootstrap*. CRC press.
- Fogg, A. R., Lester, M., Yeoman, T. K., Burrell, A. G., Imber, S. M., Milan, S. E., & Anderson, B. J. (2020). An improved estimation of SuperDARN Heppner-Maynard boundaries using AMPERE data. *Journal of Geophysical Research: Space Physics*, 125(5). <https://doi.org/10.1029/2019JA027218>
- Förster, M., Haaland, S. E., Förster, M., Feldstein, Y. I., Gromova, L. I., Dremukhina, L. A., & Haaland, S. E. (2015). Interhemispheric differences in ionospheric convection: Cluster EDI observations revisited. *Journal of Geophysical Research: Space Physics*, 120, 43–46. <https://doi.org/10.1002/2014JA020774>
- Frey, H. U., Østgaard, N., Immel, T. J., Korth, H., & Mende, S. B. (2004). Seasonal dependence of localized, high-latitude dayside aurora (HiLDA). *Journal of Geophysical Research*, 109. <https://doi.org/10.1029/2003JA010293>
- Greenwald, R. A., Baker, K. B., Dudeney, J. R., Pinnock, M., Jones, T. B., Thomas, E. C., & Yamagishi, H. (1995). DARN/SuperDARN. *Space Science Reviews*, 71, 761–796. <https://doi.org/10.1007/BF00751350>
- Haaland, S., Paschmann, G., Förster, M., Quinn, J., Torbert, R., Vaith, H., & Kletzing, C. (2008). Plasma convection in the magnetotail lobes: Statistical results from cluster edi measurements. *Annales Geophysicae*, 26, 2371–2382. <https://doi.org/10.5194/angeo-26-2371-2008>

- Haaland, S. E., Paschmann, G., Förster, M., Quinn, J. M., Torbert, R. B., McIlwain, C. E., & Kletzing, C. A. (2007). High-latitude plasma convection from cluster EDI measurements: Method and IMF-dependence. *Annales Geophysicae*, 25, 239–253. <https://doi.org/10.5194/angeo-25-239-2007>
- Hepner, J. P., & Maynard, N. C. (1987). Empirical high-latitude electric field models. *Journal of Geophysical Research*, 92, 4467–4489. <https://doi.org/10.1029/JA092iA05p04467>
- Holappa, L., Asikainen, T., & Mursula, K. (2020). Explicit IMF B_y dependence in geomagnetic activity: Modulation of precipitating electrons. *Geophysical Research Letters*, 47(4), 1–7. <https://doi.org/10.1029/2019gl086676>
- Holappa, L., & Mursula, K. (2018). Explicit IMF B_y dependence in high-latitude geomagnetic activity. *Journal of Geophysical Research: Space Physics*, 123, 4728–4740. <https://doi.org/10.1029/2018JA025517>
- Khurana, K., Walker, R., & Ogino, T. (1996). Magnetospheric convection in the presence of interplanetary magnetic field B_y : A conceptual model and simulations. *Journal of Geophysical Research*, 101, 4907–4916. <https://doi.org/10.1029/95JA03673>
- King, J. H., & Papitashvili, N. E. (2005). Solar wind spatial scales in and comparisons of hourly wind and ACE plasma and magnetic field data. *Journal of Geophysical Research*, 110(A2), A02104. <https://doi.org/10.1029/2004JA010649>
- Koustov, A. V., Yakymenko, K. N., & Ponomarenko, P. V. (2017). Seasonal effect for polar cap sunward plasma flows at strongly northward IMF B_z . *Journal of Geophysical Research: Space Physics*, 122(2), 2530–2541. <https://doi.org/10.1002/2016JA023556>
- Laakso, H., Perry, C., McCaffrey, S., Herment, D., Allen, A. J., Harvey, C. C., & Turner, R. (2010). Cluster active archive: Overview. *Astrophysics and Space Science Proceedings*, 11, 3–37. https://doi.org/10.1007/978-90-481-3499-1_1
- Lockwood, M., Owens, M. J., Barnard, L. A., Haines, C., Scott, C. J., McWilliams, K. A., & Coxon, J. C. (2020). Semi-annual, annual and Universal Time variations in the magnetosphere and in geomagnetic activity: 1. Geomagnetic data. *Journal of Space Weather and Space Climate*, 10. <https://doi.org/10.1051/swsc/2020023>
- Milan, S. E. (2015). Sun et Lumière: Solar wind-magnetosphere coupling as deduced from ionospheric flows and polar auroras. In S. W. H. Cowley FRS, D. Southwood, & S. Mitton (Eds.), *Magnetospheric plasma physics: The impact of Jim Dungey's research* (pp. 33–64). Springer International Publishing. https://doi.org/10.1007/978-3-319-18359-6_2
- Milan, S. E. (2019). AMPERE R1/R2 FAC radii. *Figshare. Dataset*. <https://doi.org/10.25392/leicester.data.11294861.v1>
- Milan, S. E., Baddeley, L. J., Lester, M., & Sato, N. (2001). A seasonal variation in the convection response to IMF orientation. *Geophysical Research Letters*, 28(3), 471–474. <https://doi.org/10.1029/2000GL012245>
- Milan, S. E., Carter, J. A., Bower, G. E., Imber, S. M., Paxton, L. J., Anderson, B. J., et al. (2020). Dual-lobe reconnection and horse-collar auroras. *Journal of Geophysical Research: Space Physics*, 10125(10). <https://doi.org/10.1029/2020JA028567>
- Milan, S. E., Carter, J. A., Korth, H., & Anderson, B. J. (2015). Principal component analysis of Birkeland currents determined by the Active Magnetosphere and Planetary Electrodynamics Response Experiment. *Journal of Geophysical Research: Space Physics*, 120(12), 10415–10424. <https://doi.org/10.1002/2015JA021680>
- Milan, S. E., Gosling, J. S., & Hubert, B. (2012). Relationship between interplanetary parameters and the magnetopause reconnection rate quantified from observations of the expanding polar cap. *Journal of Geophysical Research*, 117(A3), A03226. <https://doi.org/10.1029/2011JA017082>
- Newell, P. T., Ruohoniemi, J. M., & Meng, C.-I. (2004). Maps of precipitation by source region, binned by IMF, with inertial convection streamlines. *Journal of Geophysical Research*, 109(A10), 1–20. <https://doi.org/10.1029/2004JA010499>
- Nishida, A., Mukai, T., Yamamoto, T., Kokubun, S., & Maezawa, K. (1998). A unified model of the magnetotail convection in geomagnetically quiet and active times. *Journal of Geophysical Research*, 103(97), 4409. <https://doi.org/10.1029/97JA01617>
- Ohma, A., Østgaard, N., Reistad, J. P., Tenfjord, P., Laundal, K. M., Snekvik, K., & Fillingim, M. O. (2018). Evolution of asymmetrically displaced footpoints during substorms. *Journal of Geophysical Research: Space Physics*, 123. <https://doi.org/10.1029/2018JA025869>
- Ohma, A., Reistad, J. P., & Hatch, S. M. (2021). Modulation of magnetospheric substorm frequency: Dipole tilt and IMF B_y effects. *Journal of Geophysical Research: Space Physics*, 126(3). <https://doi.org/10.1029/2020JA028856>
- Østgaard, N., Reistad, J. P., Tenfjord, P., Laundal, K. M., Rexer, T., Haaland, S. E., & Ohma, A. (2018). The asymmetric geospace as displayed during the geomagnetic storm on 17 August 2001. *Annales Geophysicae*, 36, 1577–1596. <https://doi.org/10.5194/angeo-36-1577-2018>
- Paschmann, G., Melzner, F., Frenzel, R., Vaith, H., Parigger, P., Pagel, U., & Whipple, E. C. (1997). The electron drift instrument for cluster. *Space Science Reviews*, 1159. <https://doi.org/10.1023/A:1004917512774>
- Pettigrew, E. D., Shepherd, S. G., & Ruohoniemi, J. M. (2010). Climatological patterns of high-latitude convection in the Northern and Southern hemispheres: Dipole tilt dependencies and interhemispheric comparisons. *Journal of Geophysical Research*, 115(7), 1–15. <https://doi.org/10.1029/2009JA014956>
- Reiff, P. H., & Burch, J. L. (1985). IMF B_y -dependent plasma flow and Birkeland currents in the dayside magnetosphere. 2. A global model for northward and southward IMF. *Journal of Geophysical Research*, 90, 1595–1609. <https://doi.org/10.1029/JA090iA02p01595>
- Reistad, J. P., Laundal, K. M., Ohma, A., Moretto, T., & Milan, S. E. (2020). An Explicit IMF B_y dependence on solar wind-magnetosphere coupling. *Geophysical Research Letters*, 47(1). <https://doi.org/10.1029/2019GL086062>
- Reistad, J. P., Laundal, K. M., Østgaard, N., Ohma, A., Haaland, S., Oksavik, K., & Milan, S. E. (2019). Separation and quantification of ionospheric convection sources: 1. A new technique. *Journal of Geophysical Research: Space Physics*, 124. <https://doi.org/10.1029/2019JA026634>
- Reistad, J. P., Laundal, K. M., Østgaard, N., Ohma, A., Thomas, E. G., Haaland, S., & Milan, S. E. (2019). Separation and quantification of ionospheric convection sources: 2. The dipole tilt angle influence on reverse convection cells during northward IMF. *Journal of Geophysical Research: Space Physics*, 124. <https://doi.org/10.1029/2019JA026641>
- Reistad, J. P., Østgaard, N., Tenfjord, P., Laundal, K. M., Snekvik, K., Haaland, S., & Grocott, A. (2016). Dynamic effects of restoring footpoint symmetry on closed magnetic field-lines. *Journal of Geophysical Research: Space Physics*, 121, 1–14. <https://doi.org/10.1002/2015JA022058>
- Richmond, A. D. (1995). Ionospheric electrodynamics using magnetic apex coordinates. *Journal of Geomagnetism and Geoelectricity*, 47, 191–212. <https://doi.org/10.5636/jgg.47.191>
- Ruohoniemi, J. M., & Baker, K. B. (1998). Large-scale imaging of high-latitude convection with Super Dual Auroral Radar Network HF radar observations. *Journal of Geophysical Research*, 103(A9), 20797. <https://doi.org/10.1029/98JA01288>
- Sandholt, P. E., Moen, J., Stauning, P., Holtet, J. A., Cowley, S. W., Lockwood, M., & Egeland, A. (1998). Temporal and spatial variability of auroral forms in the 10–14 MLT sector: Relationship to plasma convection and solar wind-magnetosphere coupling. *Earth Planets and Space*, 50(8), 663–682. <https://doi.org/10.1186/BF03352161>
- Shepherd, S. G., & Ruohoniemi, J. M. (2000). Electrostatic potential patterns in the high-latitude ionosphere constrained by SuperDARN measurements. *Journal of Geophysical Research*, 105(A10), 23005–23014. <https://doi.org/10.1029/2000JA000171>

- Tenfjord, P., Østgaard, N., Haaland, S., Snekvik, K., Laundal, K. M., Reistad, J. P., & Ohma, A. (2018). How the IMF B_y induces a local B_y component during northward IMF B_z and characteristic timescales. *Journal of Geophysical Research: Space Physics*, 123, 3333–3348. <https://doi.org/10.1002/2018JA025186>
- Tenfjord, P., Østgaard, N., Snekvik, K., Laundal, K. M., Reistad, J. P., Haaland, S., & Milan, S. E. (2015). How the IMF B_y induces a B_y component in the closed magnetosphere and how it leads to asymmetric currents and convection patterns in the two hemispheres. *Journal of Geophysical Research: Space Physics*, 120. <https://doi.org/10.1002/2015JA021579>
- Thomas, E. (2020). *SuperDARN grid files used to create the Thomas and Shepherd [2018] statistical convection model*. <https://doi.org/10.5281/zenodo.3618607>
- Thomas, E. G., & Shepherd, S. G. (2018). Statistical patterns of ionospheric convection derived from mid-latitude, high-latitude, and polar SuperDARN HF radar observations. *Journal of Geophysical Research: Space Physics*, 123. <https://doi.org/10.1002/2018JA025280>
- Tikhonov, A. N., Goncharsky, A., Stepanov, V., & Yagola, A. G. (2013). *Numerical methods for the solution of ill-posed problems*. Springer Science & Business Media.
- Trattner, K. J., Petrinec, S. M., Fuselier, S. A., & Phan, T. D. (2012). The location of reconnection at the magnetopause: Testing the maximum magnetic shear model with THEMIS observations. *Journal of Geophysical Research*, 117(1), 1–12. <https://doi.org/10.1029/2011JA016959>
- Tsyganenko, N. A. (2002a). A model of the near magnetosphere with a dawn-dusk asymmetry 1. Mathematical structure. *Journal of Geophysical Research*, 107(A8), 1–17. <https://doi.org/10.1029/2001JA000219>
- Tsyganenko, N. A. (2002b). A model of the near magnetosphere with a dawn-dusk asymmetry 2. Parameterization and fitting to observations. *Journal of Geophysical Research*, 107(A8), 1–17. <https://doi.org/10.1029/2001JA000219>
- Vanhamäki, H., & Juusola, L. (2020). Introduction to spherical elementary current systems. In M. Dunlop, & H. Lühr (Eds.), *Ionospheric multi-spacecraft analysis tools: Approaches for deriving ionospheric parameters* (pp. 5–33). https://doi.org/10.1007/978-3-030-26732-2_2
- Wilder, F. D., Clauer, C. R., & Baker, J. B. (2008). Reverse convection potential saturation during northward IMF. *Geophysical Research Letters*, 35(12). <https://doi.org/10.1029/2008GL034040>
- Wilder, F. D., Clauer, C. R., & Baker, J. B. H. (2010). Polar cap electric field saturation during interplanetary magnetic field B_z north and south conditions. *Journal of Geophysical Research*, 115(A10), A10230. <https://doi.org/10.1029/2010JA015487>
- Yakymenko, K. N., Koustov, A. V., & Fiori, R. A. (2018). Interhemispheric asymmetry of the sunward plasma flows for strongly dominant IMF $B_z > 0$. *Journal of Geophysical Research: Space Physics*, 123(1), 315–325. <https://doi.org/10.1002/2017JA024644>